A simple ballistic material model for soda-lime glass

M. Grujicic [a,*], B. Pandurangan [a], N. Coutris [a], B.A. Cheeseman [b], C. Fountzoulas [b], P. Patel [b], D.W. Templeton [c], K.D. Bishnoi [c]

[a] International Center for Automotive Research CU-ICAR, Department of Mechanical Engineering, Clemson University, 241 Engineering Innovation Building, Clemson, SC 29634-0921, United States
[b] Army Research Laboratory – Survivability Materials Branch, Aberdeen, Proving Ground, MD 21005-5069, United States
[c] US Army TARDEC, AMSRD-TAR-R/MS 263, Warren, MI 48397-5000, United States

ARTICLE INFO

ABSTRACT

Various open-literature experimental findings pertaining to the ballistic behavior of glass are used to construct a simple, physically based, high strain-rate, high-pressure, large-strain constitutive model for this material. The basic components of the model are constructed in such a way that the model is suitable for direct incorporation into standard commercial transient non-linear dynamics finite-element based software packages like ANSYS/Autodyn [ANSYS/Autodyn version 11.0, User documentation, Century Dynamics Inc. a subsidiary of ANSYS Inc.; 2007.] or ABAQUS/Explicit [ABAQUS version 6.7, User documentation, Dessault systems, 2007.]. To validate the material model, a set of finite element analyses of the Edge-on-Impact (EOI) tests is carried out and the results compared with their experimental counterparts obtained in the recent work of Strassburger et al. [Strassburger E, Patel P, McCauley JW, Kovalchick C, Ramesh KT, Templeton DW. High-speed transmission shadowgraphic and dynamic photoelasticity study of stress wave and impact damage propagation in transparent materials and laminates using the edge-on impact method. In: Proceedings of the twenty-third international symposium on ballistics. Spain: April 2007, and Strassburger E, Patel P, McCauley W, Templeton DW. Visualization of wave propagation and impact damage in a polycrystalline transparent ceramic-AlON. In: Proceedings of the twenty-second international symposium on ballistics. Vancouver, Canada: November 2005.]. Overall, a good agreement is found between the computational and the experimental results pertaining to: (a) the front-shapes and propagation velocities of the longitudinal and transverse waves generated in the target during impact; (b) the front-shapes and propagation velocities of the "coherent-damage" zone (a zone surrounding the projectile/target contact surface which consists of numerous micron- and sub-micron-size cracks); and (c) the formation of "crack centers", i.e. isolated cracks nucleated ahead of the advancing coherent-damage zone front. Relatively minor discrepancies between the computational and the experimental results are attributed to the effects of damage-promoting target-fixturing induced stresses and cutting/grinding-induced flaws located along the narrow faces of the target and the surrounding regions.

1. Introduction

The critical importance of armor (including transparent armor) has become evident by recent experiences of the U.S. military forces in the Operation Iraqi Freedom. With continuing escalations in the number and variety of threats, the needs for rapidly deployable threat-specific weight/cost-performance-optimized transparent-armor and armor systems have greatly increased. There are numerous efforts by the researchers in the U.S.A. and elsewhere around the world, to help accelerate the development of transparent-armor systems. Traditionally, transparent armor is made of monolithic glass or transparent-elastomer inter-layered glass laminates. Among the new transparent-armor materials and technologies available today, the following have received most attention: crystalline ceramics (e.g. aluminum-oxinitride spinel, AlON [4]), new transparent polymer materials (e.g. transparent nylon [5]), and new interlayer technologies (e.g. polyurethane bonding layers [3]), and new laminate designs (e.g. [6]). Due to their large size and curved shape, the majority of armor windows are still being constructed using glass. While ever increasing demands for reductions in weight and for improvements in ballistic-protection performance of transparent armor are calling for the use of new transparent materials (e.g. transparent crystalline ceramics, advanced transparent polymeric materials) and advanced technologies (e.g. multi-material functionally graded laminated

* Corresponding author. Tel.: +1 864 656 5639; fax: +1 864 656 4435.
E-mail address: mica.grujicic@ces.clemson.edu (M. Grujicic).

1. REPORT DATE **2009**	2. REPORT TYPE		3. DATES COVERED **00-00-2009 to 00-00-2009**
4. TITLE AND SUBTITLE **A simple ballistic material model for soda-lime glass**		5a. CONTRACT NUMBER	
		5b. GRANT NUMBER	
		5c. PROGRAM ELEMENT NUMBER	
6. AUTHOR(S)		5d. PROJECT NUMBER	
		5e. TASK NUMBER	
		5f. WORK UNIT NUMBER	
7. PERFORMING ORGANIZATION NAME(S) AND ADDRESS(ES) **Celmson University,Department of Mechanical Engineering,Clemson,SC,29634**		8. PERFORMING ORGANIZATION REPORT NUMBER	
9. SPONSORING/MONITORING AGENCY NAME(S) AND ADDRESS(ES)		10. SPONSOR/MONITOR'S ACRONYM(S)	
		11. SPONSOR/MONITOR'S REPORT NUMBER(S)	
12. DISTRIBUTION/AVAILABILITY STATEMENT **Approved for public release; distribution unlimited**			
13. SUPPLEMENTARY NOTES			

14. ABSTRACT

Various open-literature experimental findings pertaining to the ballistic behavior of glass are used to construct a simple, physically based, high strain-rate, high-pressure, large-strain constitutive model for this material. The basic components of the model are constructed in such a way that the model is suitable for direct incorporation into standard commercial transient non-linear dynamics finite-element based software packages like ANSYS/Autodyn [ANSYS/Autodyn version 11.0, User documentation, Century Dynamics Inc. a subsidiary of ANSYS Inc.; 2007.] or ABAQUS/Explicit [ABAQUS version 6.7, User documentation Dessault systems, 2007.]. To validate the material model, a set of finite element analyses of the Edge-on-Impact (EOI) tests is carried out and the results compared with their experimental counterparts obtained in the recent work of Strassburger et al. [Strassburger E, Patel P, McCauley JW Kovalchick C, Ramesh KT, Templeton DW. High-speed transmission shadowgraphic and dynamic photoelasticity study of stress wave and impact damage propagation in transparent materials and laminates using the edge-on impact method. In: Proceedings of the twenty-third international symposium on ballistics. Spain: April 2007, and Strassburger E, Patel P, McCauley W, Templeton DW. Visualization of wave propagation and impact damage in a polycrystalline transparent ceramic-AlON. In: Proceedings of the twenty-second international symposium on ballistics. Vancouver, Canada: November 2005.]. Overall a good agreement is found between the computational and the experimental results pertaining to: (a) the front-shapes and propagation velocities of the longitudinal and transverse waves generated in the target during impact; (b) the front-shapes and propagation velocities of the ??coherent-damage?? zone (a zone surrounding the projectile/target contact surface which consists of numerous micron- and submicron- size cracks); and (c) the formation of ??crack centers??, i.e. isolated cracks nucleated ahead of the advancing coherent-damage zone front. Relatively minor discrepancies between the computational and the experimental results are attributed to the effects of damage-promoting target-fixturing induced stresses and cutting/grinding-induced flaws located along the narrow faces of the target and the surrounding regions.

15. SUBJECT TERMS					
16. SECURITY CLASSIFICATION OF:			17. LIMITATION OF ABSTRACT	18. NUMBER OF PAGES	19a. NAME OF RESPONSIBLE PERSON
a. REPORT **unclassified**	b. ABSTRACT **unclassified**	c. THIS PAGE **unclassified**	**Same as Report (SAR)**	**16**	

transparent armor), glass (as well as glass ceramics) continue to remain important material choice in ground-vehicle transparent-armor applications. Compositional modifications, chemical strengthening, and controlled crystallization have demonstrated to be capable of significantly improving the ballistic properties of glass [5]. Glass windshields and windows can also be produced in large sizes with curved geometries, and can be produced to provide incremental ballistic performance at incremental cost.

The development of new glass-based transparent-armor systems aimed at reducing the vulnerability of the military vehicle occupants and on-board instrumentation to various threats typically includes extensive experimental test programs. Such experimental test programs are critical for ensuring the utility and effectiveness of the transparent-armor systems. However, the use of experimental test programs is generally expensive, time-consuming and involves destructive testing. While the role of experimental test programs remains critical, they are increasingly being complemented by the corresponding computation-based engineering analyses and simulations. The knowledge of the armor-material response under high-deformation-rate/high-pressure loading conditions, as described by the corresponding material model, is one of the key components in such analyses greatly affecting their utility and fidelity. The main objective of the present paper is to help with a further advancement of these computational engineering analyses and simulations, through the development of a simple yet physically sound material model for soda-lime glass used in transparent-armor applications. It is hoped that such advances can help the engineering analyses become a reliable method/alternative in the effective transparent-armor systems development process.

It is well established that glass exhibits quite different behavior under quasi-static (i.e. low-deformation-rate) and dynamic (i.e. high-deformation-rate) loading conditions. Under quasi-static loading conditions, pre-existing flaws/defects situated primarily in the surface regions of glass play a dominant role in the fracture process and fracture results in the formation of few large fragments [7,8]. Under dynamic loading conditions, surface flaws are often found to still play a dominant role in the fracture of glass (e.g. [9]). However, there are several observations (e.g. [3,4,10]) which suggest that high-intensity stresses may cause the nucleation of bulk/volume defects so that the fracture process becomes less surface-flaw controlled. Bulk cracks are seldom observed under quasi-static loading conditions except under very specific loading conditions (e.g. such as those encountered during high-temperature testing of glass fibers [11], compression testing of glass spheres [12], etc).

As mentioned above, brittle failure in ceramics and glasses is the result of nucleation (on pre-existing flaws) and propagation of the cracks, and it is accompanied by stress attenuation and fragments formation. Finite element analyses have been extensively used over the last dozen of years to elucidate the underlying mechanisms and quantify the ballistic performance of ceramic targets under high-velocity impact and penetration conditions. In these analyses, most of the effort was typically devoted to modeling the complicated post-failure initiation response of ceramic materials (i.e. the mechanical/structural response of these materials to impact loads in the presence of cracks). In general, all the existing brittle-fracture models reported in the literature, can be categorized as being either: (a) continuum based or (b) being of a discrete nature.

The continuum approaches (e.g. [8,13,14]) generally involve homogenization of a crack-laden (damaged) material into an equivalent crack-free continuum material with degraded stiffness and strength. The fundamental assumption in these models is that the elastic-stiffness degradation is the result of inelastic deformation caused by micron- and sub-micron-size cracks and that this degradation can be quantified using a so-called "*damage tensor*" whose evolution during loading can be formulated using a generalized Griffith-type crack initiation and propagation criteria for

brittle materials. In addition, some of continuum models account for the interactions between the cracks, their coalescence, friction between fragments, etc. However, most of these phenomenological models have short-comings in that they cannot describe damage induced anisotropy and also, that their parameters are difficult to determine experimentally. Since the continuum model proposed by Hild et al. [13,19] does not suffer from these deficiencies, it was used as a basis for the model developed in the present work.

To overcome the aforementioned limitations of the continuum models, Espinosa et al. [15,16] proposed a multiple-crack-plane (continuum) micro-mechanics constitutive model for brittle materials which can be parameterized by measuring experimentally the fundamental material properties (e.g. the grain size and fracture toughness). Within the model, the dynamic growth of micro-cracks with different orientations is considered leading to damage induced anisotropy while the rate effects are naturally incorporated in the model. In spite of these improvements, the continuum models continue to be criticized because they require assumptions regarding the size and distribution of pre-existing crack-nucleating defects, and because they cannot be used to describe the growth of dominant cracks (the cracks which lead to failure), which, due to their size, cannot bee smeared-out/homogenized. On the computational side, the continuum models suffer from the problem that at very large deformations and under high strain rates, finite-element distortions may reduce the integration time steps below an acceptable level. One of the possible means to circumvent this problem is the application of adaptive meshing (e.g. [2]), a procedure in which a region containing highly distorted elements is re-meshed, in the course of an analysis, using regularly shaped elements. However, repeated application of adaptive meshing during the analysis is also computationally quite costly.

The discrete models for brittle fracture (e.g. [17]) deal with the nucleation, propagation and coalescence of discrete (rather then smeared-out/homogenized) cracks during deformation. Among these models, the one proposed by Camacho and Ortiz [17] appears to be the most comprehensive. Within this model, conical and longitudinal cracks are allowed to nucleate at any node in a finite element mesh when the resolved normal or shear stress at that node reaches an effective fracture stress. Cracks are nucleated by duplicating nodes and propagated, along the element boundary, by continuing to duplicate nodes. Adaptive re-meshing is used to provide a reach enough set of possible fracture paths around the crack tip. The forces at the cracked surfaces are brought to zero in accordance with the Griffith criterion accounting for unloading, before reaching the critical fracture opening. This enables the formation of fragments as cracks coalesce in a closed path. Thereafter, contact and friction between the fragments are accounted for. The major disadvantages of the discrete models, such as the one described above, are that they are extremely computationally intensive and become intractable as the number of cracks increases. In order to capture all possible crack nucleating sites, meshes with micron-size element are ultimately required.

The detailed review of the continuum and discrete material models (like the ones mentioned above) carried out in the present work clearly established that these models are capable of revealing complex intrinsic mechanisms and phenomena associated with fracture in brittle materials and are, hence, very important for gaining a better understanding of the behavior of these classes of materials. However, one may argue that it is the effect of these mechanisms/phenomena on the material response and not their explicit modeling that is needed in the computationally efficient material models suitable for use in large-scale computational analyses of the ballistic performance of geometrically complex multi-layered, functional armor systems. In the present work, a simple high strain-rate, high-pressure, large-strain material model is proposed for soda-lime glass, a material which is

traditionally used in the transparent-armor systems. In the present work, the continuum model for soda-lime glass, a material typically used in transparent-armor systems, originally proposed by Hild et al. [13,19] was critically assessed and used to derive a simple high strain-rate, high-pressure, large-strain model for this material. While simplicity (i.e. computational efficiency) is the key requirement for this model, every effort is made to preserve all the underlying physics associated with the material response.

The organization of the paper is as follows: in Sections 2.1 and 2.2, brief overviews are provided of the quasi-static and dynamic failure regimes observed in brittle materials like glass. The derivation of the new material model for soda-lime glass including its physical foundation, the governing equations and the parameterization procedure is presented in Section 2. Details of a transient non-linear dynamics computational analysis of an Edge-on-Impact (EOI) test used to validate the material model for soda-lime glass are presented in Section 3. The main results obtained in the present work are presented and discussed in Section 4. The key conclusions resulted from the present work are summarized in Section 5.

2. Derivation of the material model

As discussed earlier, the main purpose of the present work is to develop a simple large-strain, high-deformation-rate, high-pressure material model for glass suitable for use in large-scale computational analysis of ballistic performance of transparent armor. While the main requirement for the material model in this case is its computational efficiency, every effort is made to retain the physical soundness of the model and address within it the key underlying physical phenomena controlling the mechanical response of glass under ballistic loading conditions. In the remainder of this section, a detailed account is presented of the essential features of the new material model for glass, the derivation procedure used to construct various components of the glass and the approach used for parameterization of the model. In addition, validation of the model against Edge-On-Impact experimental results obtained by Strassburger [3,4] is provided in the next section. In our ongoing work [21], the present material model and ANSYS/Autodyn [1], a general purpose transient nonlinear dynamics program, are being used to address the problem of multi-hit ballistic-penetration performance of a laminated glass/polycarbonate armor.

2.1. Physical foundation of the model

It is well established that the mechanical response of glass is drastically different under low-deformation-rate (i.e. quasi-static) and high-deformation-rate (i.e. dynamic) loading conditions (e.g. [18,19]). Under quasi-static loading conditions, glass typically fails by the propagation of a single or a couple of discrete cracks and only a few fragments are created after complete fracture. In sharp contrast, under dynamic loading conditions, glass tends to undergo substantial damage (resulting from the formation of a large number of micron- and sub-micron-size cracks) and tends to undergo comminution (i.e. forms a large number of sub-millimeter size fragments). In both cases, however, the failure is believed to be controlled by pre-existing flaws which, when subjected to sufficiently large stresses, can become cracks. A more quantitative overview of the two failure regimes (i.e. the quasi-static coarse-fragmentation regime and the dynamic comminution regime) is presented in the Appendix.

The occurrence of the two fracture regimes is believed to be the result of the two internal processes accompanying loading of glass: (a) crack formation at the pre-existing flaws and crack growth. The formation of cracks is accompanied by the formation of the so-called "shielding" zones, i.e. the zones surrounding the cracks within which the stresses are highly relaxed and the probability of nucleation of additional cracks is very small; and (b) the increase in stress level which promotes the formation of additional cracks (at less potent pre-existing flaws). Since the crack formation process is typically associated with mechanical instability (i.e. once a crack is nucleated, it grows at a terminal velocity, until it reaches the free surface or another crack), low loading rates tend to promote the coarse-fragmentation fracture regime. In other words, once a crack or a couple of cracks are formed, they can extend over the entire structure before the stress at other flaws has reached a high enough level to form additional cracks. Conversely, high loading rates promote the formation of large number of cracks, i.e. the critical stress level for crack nucleation is reached at many pre-existing flaws before the previously nucleated cracks have a chance to extend far enough and shield these flaws from the externally applied stress.

In the Edge-on-Impact (EOI) tests, reviewed in more details in Section 3.1, it is also observed that both regimes of fragmentation take place, i.e. in the region of the glass-plate target surrounding the projectile-impacted surface, in which the loading rates are very high, fracture is dominated by the fine-scale ("coherent") damage and the comminution (with occasional appearance of few course fragments). On the other hand, in target regions further away from the impact surface in which the loading rate is relatively low, isolated "crack centers" are formed and grow until they are swept by the advancing coherent-damage (i.e. the comminution) front.

2.2. Simplifying assumptions and basic components of the model

In this section, more details are provided regarding the development of the new ballistic material model for glass. The following are the key simplifying assumptions and basic components of the model:

(a) The distribution of pre-existing flaws throughout the material is assumed to follow the Weibull-type distribution, see the Appendix. In order to account for the differences in the flaw distributions between the target surface and the bulk, different (typical) Weibull distribution parameters for soda-lime glass are used when dealing with surface and near-surface regions vs. the bulk region of the material, Table 1. The data listed in Table 1 were compiled using experimental results obtained in several investigations (e.g. [9,19]);

(b) Both the nucleation of micro-cracks (which leads to comminution) and macro-cracks (which leads to coarse fragmentation) are governed by the same stress-level based damage initiation criterion. Crack initiation is assumed to be controlled by the largest principal normal stress and only the normal mode (mode I) of cracking is considered;

Table 1
Mechanical property parameters for soda-lime glass used in the present work

Property	Symbol	Value	Unit
Young's modulus	E	70.0	GPa
Poisson's ratio	ν	0.22	N/A
Density	ρ	2500	kg/m^3
Surface controlled fracture			
Weibull modulus	m	7	N/A
Mean static fracture strength	$\sigma_{f,static}$	50	MPa
Effective surface	Z_{eff}	0.024	m^2
Volume controlled fracture			
Weibull modulus	m	30	N/A
Mean static fracture strength	$\sigma_{f,static}$	230	MPa
Effective volume	Z_{eff}	10^{-4}	m^3

(c) It is further assumed that it is the loading/stress rate at the moment of crack nucleation which determines if a crack will be a single macro-crack within a given finite element leading to its coarse-fragmentation failure mode or the crack will be accompanied by the formation of many additional micro-cracks leading to progressive damage and ultimate multiple-fragmentation failure of the element. A single critical stress-rate value will be used to separate these two regimes of fracture. In accordance with the model-development procedure, numerical implementation of the model and the results displayed in Fig. A1 in the Appendix, this critical stress-rate, $\dot{\sigma}_{crit}$, is set to a value of 1,000 MPa/μs. At stress rates below this critical value, single crack fracture regime will be assumed while at stress rates larger than the critical value a multiple-crack regime will be assumed;

(d) When a single crack is nucleated within an element, this crack extends at the terminal velocity (please see Eq. (A.7) in the Appendix) and the total time for element failure is obtained by dividing the characteristic element dimension by the terminal crack velocity. Once an element is fractured in a single-crack mode, it is removed from the model. The employed element-deletion approach may significantly affect the subsequent results pertaining to the temporal evolution and spatial distribution of deformation and damage. To investigate the potential effect of the element-deletion procedure used, few analyses were carried out in which "*failed elements*" were retained. Except for excessive deformation of the failed elements, no significant differences were observed in the results obtained using the two types of analyses. In other words, multi-axial macro-cracking is not handled explicitly. When an element is undergoing fracture due to the growth of a single-crack, stiffness and strength properties of this element are degraded linearly with the corresponding crack strain from the point of crack initiation to the point of complete traversal of the element by the crack;

(e) Once an element has started undergoing ("*coherent*") damage due to the formation of multiple cracks, stress-shielding and path-crossing effects initially prevent the nucleation of macro-cracks. However, when the extent of coherent damage within a single element reaches a critical value, this element is assume to fracture by micro-crack coalescence and to loose most of its ability to support load. To account for the experimental observations that the resulting micro-fragments remain confined by the surrounding non-fractured material and can support compressive and shear loads, the elements that failed in the multi-fragmentation regime are not removed from the model. Instead, they are retained and assigned small residual normal and shear stiffness values. The stress-rate invariant critical level of coherent damage is computed using Eq. (A.22);

(f) When an element is subjected to coherent damage, the extent of damage is governed by a damage evolution equation and the degradation of the corresponding stiffness and stress properties of the material are governed by the appropriate damage-dependent stiffness and strength relations. The rate of change of the extent of damage, D, with maximum principal stress, σ, is obtained by differentiating Eq. (A.14) to get:

$$dD/d\sigma = \frac{m!n!(m+n)\sigma^{m+n-1}}{(m+n)!\sigma_c^{m+n}}(1-D) \qquad (1)$$

please refer to the Appendix for the explanation of the symbols used in Eq. (1). It should be noted that, Eq. (1) is strictly valid only under constant stress-rate loading conditions and when the maximum principal stress is tensile and greater than the

"*damaged*" material strength. Coherent damage, as implied by Eq. (1), is assumed to be isotropic and, hence, degraded glass, like the virgin glass, is considered as an isotropic material. Degradation of the Young's modulus of the glass is then defined by the following relation:

$$E = E_0(1-D) \qquad (2)$$

where subscript 0 is used to denote a quantity pertaining to glass in its initial condition.

One of the key features of the present model is that, in the fine-fragmentation regime and in accordance with Eq. (1), the evolution of coherent damage is controlled by the "*internal*" stress, σ (i.e. the stress residing in the non-shielded portion of the finite element in question, while the overall stress state at that element is defined by a "*macroscopic*" stress, $\Sigma = \sigma(1 - D(\sigma))$). Clearly the internal-stress level is controlled by the initial stiffness of soda-lime glass while the macroscopic-stress level is controlled by the degraded-material stiffness.

(g) It is customary in many dynamic material models to separately define an equation of state (a function which relates pressure to the mass density and the internal energy density and strength/failure functions) which describe the evolution of the deviatoric part of stress during plastic deformation and damage/fracture. In the present work, a linear equation of state with a damage-sensitive bulk modulus was used, while no account was given to the phenomenon of bulking; and

(h) The proposed model for soda-lime glass is temperature insensitive. In other words, potential strain softening effects which can occur during impact of a projectile onto a glass panel are not considered.

2.3. Parameterization of the model

As discussed earlier brittle failure of glass in either of the coarse-fragmentation or fine-fragmentation mode is assumed to be controlled by pre-existing defects and to comply with the Weibull distribution. However, to account for the fact that surface regions can contain higher density of flaws, different Weibull distribution parameters were used for the finite elements residing on the target faces, Table 1. Table 1 also contains the values for the linear elastic properties of soda-lime glass. As stated in the previous section, transition between the coarse-fragmentation and fine-fragmentation brittle-fracture modes is assumed to take place at a constant stress-rate, which, based on Fig. A1 is set to 1,000 MPa/μs. A typical value of 0.3 is assigned to the ratio between the crack terminal velocity and the sound speed, k. The crack shielding zones are assumed to be circular or spherical depending on whether the failure is controlled by surface or volume flaws.

2.4. Implementation of the material model in a user-material subroutine

The brittle-fracture material model for soda-lime glass developed and parameterized in the previous sections is next implemented in a *VUMAT Material User Subroutine* of the commercial finite element program ABAQUS/Explicit [2]. This subroutine is compiled and linked with the finite element solver and enables ABAQUS/Explicit to obtain the needed information regarding the state of the material and the material mechanical response during each time step, for each integration point of each element.

The essential features of the coupling between the ABAQUS/Explicit finite-element solver and the VUMAT Material User Subroutine at each time increment at each integration point of each element can be summarized as follows:

(a) The corresponding previous time-increment stresses and material state variables as well as the current time-step strain increments are provided by the ABAQUS/Explicit finite-element solver to the material subroutine. In the present work, the strain components, the extent of coherent damage and a variable defining the deletion status of the element in question are used as state variables; and

(b) Using the information provided in (a), and the meso-scale unit-cell used material model presented in the previous section, the material stress state as well as values of the material state variables at the end of the time increment are determined within the VUMAT and returned to the ABAQUS/Explicit finite-element solver. In addition, the changes in the total internal and the inelastic energies (where appropriate) are computed and returned to the solver.

3. Validation of the material model

The material model for soda-lime glass developed and parameterized in the previous section is validated in this section by carrying out a series of transient non-linear dynamics analyses of the Edge-on-Impact tests of a glass target and by comparing the computational results with the experimental results obtained recently by Strassburger et al. [3,4]. In the remainder of this section, a brief description of the EOI test and the nature of the results obtained in this test are presented. This is followed by the description of the computational procedure used to simulate the test.

3.1. Edge-on Impact test

3.1.1. Test set-up and procedure
Edge-on Impact (EOI) tests are frequently used to study the deformation and damage of (non-transparent) conventional structural-ceramic armor systems and involves real-time, reflection-mode, optical monitoring of the armor deformation and damage during impact. In the recent work of Strassburger et al. [3,4], the EOI set-up is coupled with a high-speed 0.10 µs-resolution Cranz-Schardin camera and utilized in a number of studies to visualize damage propagation and dynamic fracture in structural ceramics. Strassburger et al. [3,4] also reconfigured the EOI test set-up in order to record photographically the evolution of damage in transparent-armor systems using the plane-light shadow-graphs transmission mode ("*the shadow-graphs mode*"). In addition, the test set-up was modified by adding crossed polarizers to visualize the propagation of stress waves using a dynamic photo-elasticity technique ("*the photo-elasticity mode*"). A schematic of the EOI test set-up with the added crossed polarizers is displayed in Fig. 1. A close-up view of the projectile/target interaction and a schematic of the resulting damage and wave-swept zones are provided in Fig. 2.

In the work of Strassburger et al. [3,4], a projectile is used to strike one side face (generally referred to as an "*edge*") of a plate-like specimen/target and damage formation and fracture propagation is recorded by photographing (in transparent mode) the broad faces of the target during the first 20 µs following the impact. Plate-shape $100 \times 100 \times 10$ mm test specimens/targets are typically impacted using either solid cylinder-shape steel projectiles (30 mm diameter, 23 mm length) or using 16 mm-diameter solid sphere-shaped projectiles. The impact velocities used are normally in a range between 270 and 925 m/s. In the shadow-graph mode of the optical set-up, the target is placed between the condensing lens and the camera. In the photo-elasticity mode of the optical set-up, two sheet polarizers (one on each side of the target) are attached to the transparent sides of the target chamber so that broad polarizers' faces are parallel with the broad target faces, Fig. 1.

To help clarify the nature of the shadow-graph type and the photo-elasticity type EOI results, simple schematics of these results
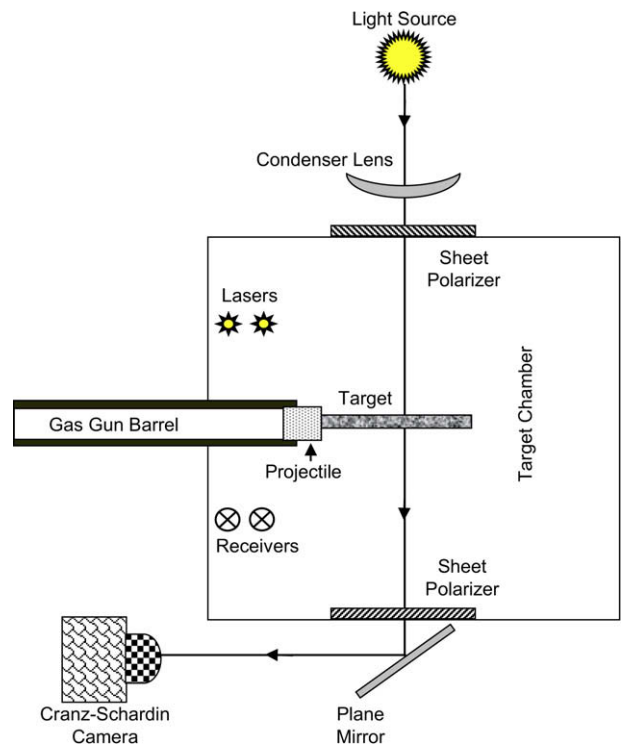

Fig. 1. A schematic of the Edge-on-Impact (EOI) experimental set-up with two cross polarizers and a single Cranz-Schardin camera.

are provided in Fig. 3(a) and (b), respectively. Schematics shown in Fig. 3(a) and (b) both pertain to the corresponding photographic positives, i.e. due to the damage induced, the coherent damage zone as well as the isolated crack centers appear as dark regions in the shadow-graphs. Differences in the light intensity associated with the longitudinal-wave and transverse-wave swept regions in the case of shadow-graph mode are dominated by stress-induced birefringence effects (in the case of the longitudinal wave) and by surface reflection phenomena (in the case of the transverse wave). In the case of the photo-elastic imaging mode, stress-induced birefringence in the target material gives rise to a 90° switching in the beam polarization vector producing bright regions in the stressed areas.
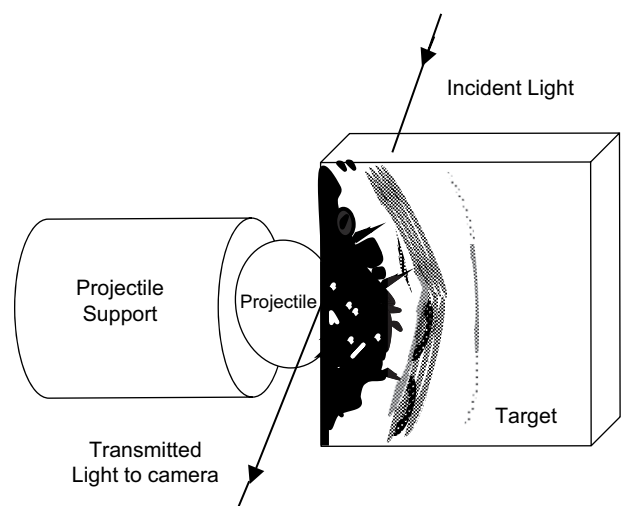

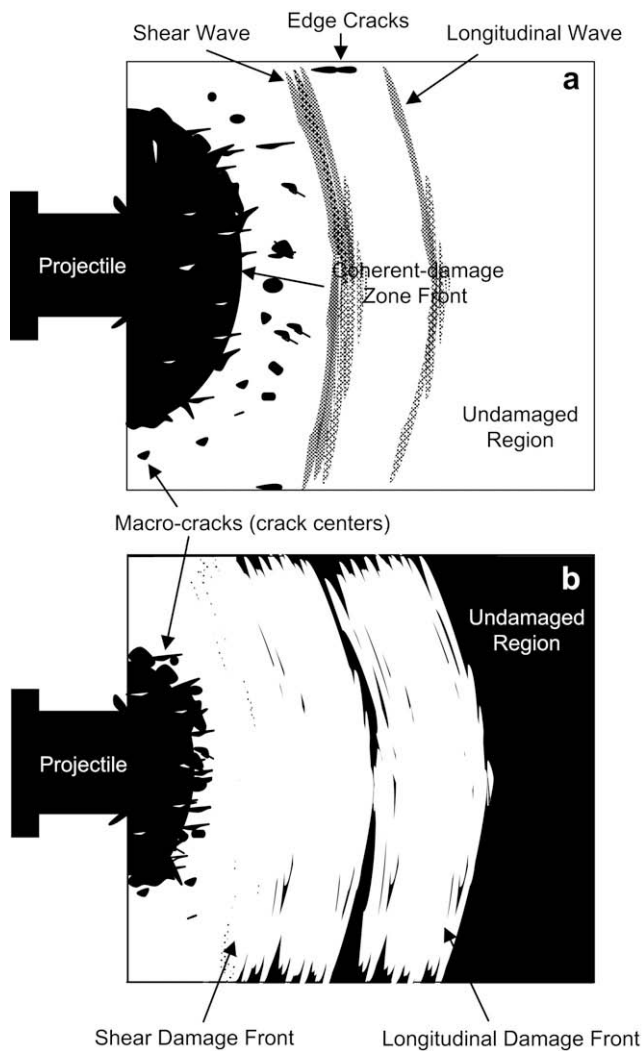**Fig. 2.** A close-up view of the projectile/target interaction in an EOI set-up.

Fig. 3. Schematic of the typical (a) shadow-graph and (b) birefringence results obtained in the work by Strassburger et al. [3,4].

3.1.2. Typical EOI test results for soda-lime glass

As discussed in the previous section, two different optical configurations were employed in the work of Strassburger et al. [3,4]: (a) a regular transmitted plane-light shadow-graph set-up was used to observe wave and damage propagation, while a modified configuration, in which the specimens were placed between crossed polarizers to create a photo-elastic effect, was used to visualize the stress-wave propagation. Pairs of impact tests at approximately identical velocities were conducted in transmitted plane (shadow-graphs) and crossed polarized light. The two sets of results were next compared to establish the extent of wave and damage propagation and to establish correlation between damage initiation and the stress components most likely responsible for the observed damage.

The main observations made by Strassburger et al. [3,4], during the EOI testing of soda-lime glass can be summarized as follows:

(a) Damage appears to be in two distinct forms: (i) as a coherent, continuous (damage) zone emanating from the impacted target edge and (ii) as discrete crack centers located at some distance from the advancing coherent-damage zone front. To overcome the limitations of the "*side-view*" shadow-graph optical set-up that always provides photographic images with superimposed bulk-damage and surface-damage

contributions, Strassburger et al. [3,4] also carried out a simultaneous top-view shadow-graph imaging of the target-damage process. The results obtained revealed that the material damage initiates both in the bulk of the target and on the side faces. The advancement of damage from the impacted edge of the specimen was found to be greater in the case of bulk-damage. This finding was somewhat surprising since, in the case of glass, it is generally postulated that damage-inducing flaws are primarily concentrated in the surface regions of the sample;

(b) While both the shadow-graph optical mode and the photo-elastic mode revealed the positions of the advancing longitudinal and shear waves, the positions of the wave front revealed by the two optical set-ups were somewhat different. This discrepancy was explained to be the result of differences in the physical phenomena responsible for the light-intensity differences (contrast) in the two cases. That is, in the case of plain-light shadow-graph optical set-up, the transmitted-light intensity is controlled by the second derivative of the refractive index while in the case of cross-polarizers set-up, the transmitted-light intensity is controlled by the underlying photo-elastic effect;

(c) The longitudinal-wave velocity was found to be around 5760 m/s while the propagation velocity of the transverse waves was found to be ca. 3520 m/s. Both of these velocities are consistent with their counterparts (5708 m/s and 3224 m/s) computed using the Young's modulus of 73 GPa, a shear modulus of 29 GPa and a density of 2240 kg/m^3 for glass [16]; and

(d) The damage propagation velocity (defined as the velocity at which new crack centers are nucleated ahead of the advancing coherent-damage zone front) was found to be ca. 3270 m/s and thus quite close to the transverse-wave velocity. This finding suggests that the most likely mechanism for damage initiation is transverse/hoop normal stress-induced radial-crack formation at pre-existing material flaws.
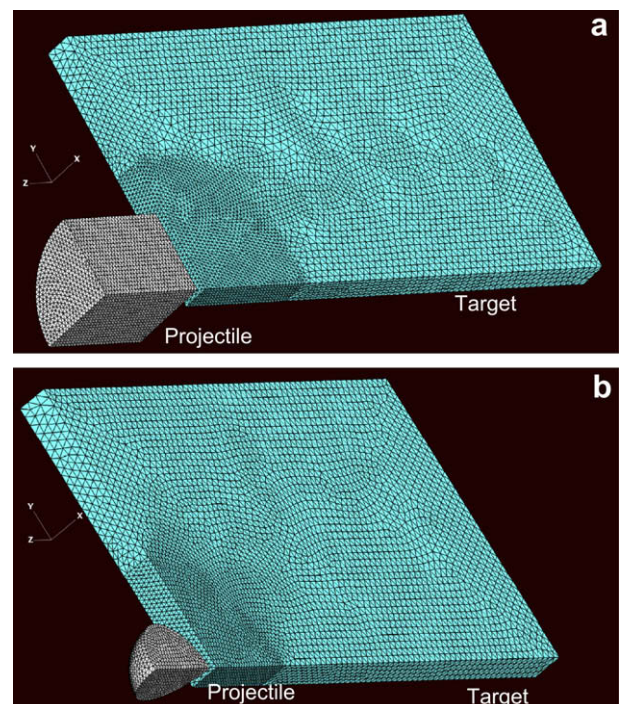

Fig. 4. Typical (quarter) meshed models used for the projectiles and the target.

3.2. Transient non-linear dynamics analysis of the EOI test

In this section, a brief description is provided regarding the construction of the geometrical model and the computational procedure used to simulate the Edge-on-Impact tests on soda-lime glass as carried out by Strassburger et al. [3,4].

Plate-like soda-lime glass targets with $L \times W \times H = 100$ mm $\times 100$ mm $\times 10$ mm dimensions are used and one of their edges is impacted with either a 4340-steel spherical projectile (diameter = 16 mm) or a 4340-steel cylindrical projectile (diameter = 30 mm, height = 23 mm). Both the target and the projectile were initially meshed using four-node reduced integration tetrahedron solid elements. Since initial work showed that no plastic deformation takes place in the projectile during impact, 4340 steel was modeled as a linear elastic material with a Young's modulus $E = 210$ GPa and a Poisson's ratio $\nu = 0.3$. The soda-lime glass target was modeled using the high-deformation-rate, high-pressure, large-strain model presented in the previous section. To capture the details of the projectile-target interaction, finer mesh was used in the target region near the impacted side face. Also, since only the normal impact of the projectile on the target is analyzed, an advantage is taken of the inherent symmetry of the model, i.e. only one quarter of the model is analyzed. Typically the spherical and the cylindrical projectiles were divided into ~8000 and ~27,000 elements, while the target contained ~72,000 elements. The edge length of the target elements near the impacted face was ca. 0.25 mm. Examples of the typical meshed models used in the present work are displayed in Fig. 4(a) and (b). The mesh size was varied initially in order to validate that the results are not significantly mesh-size dependent.

All the calculations were carried out using ABAQUS/Explicit computer program [2]. The material model for the soda-lime glass was implemented into a *VUMAT* User Material Subroutine and linked with ABAQUS/Explicit before the model could be used.

Interactions between the projectile and the target as well as between different fragments of the target are modeled using the "*Hard Contact Pair*" type of contact algorithm. Within this algorithm, contact pressures between two bodies are not transmitted unless the nodes on the "*slave surface*" contact the "*master surface*". No penetration/over closure is allowed and there is no limit to the magnitude of the contact pressure that could be transmitted when the surfaces are in contact. Transmission of shear stresses across the contact interfaces is defined using a simple Coulomb model based on a 0.15 static, μ_{st}, and a 0.10 kinematic, μ_{kin}, friction coefficient and a 170 MPa upper-bound shear stress limit, τ_{slip} (a maximum
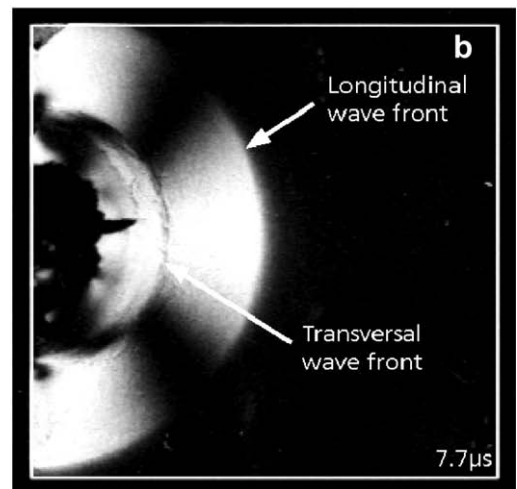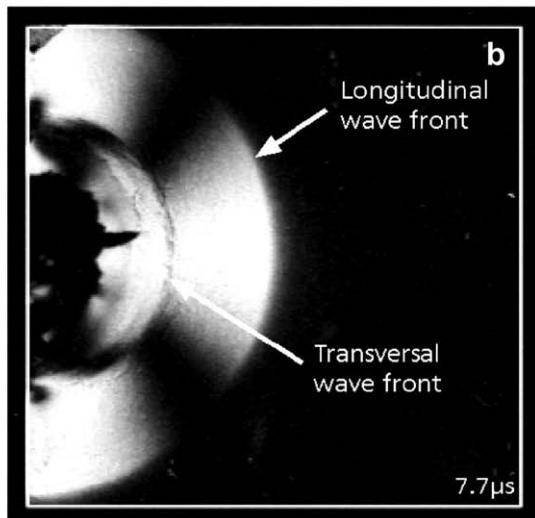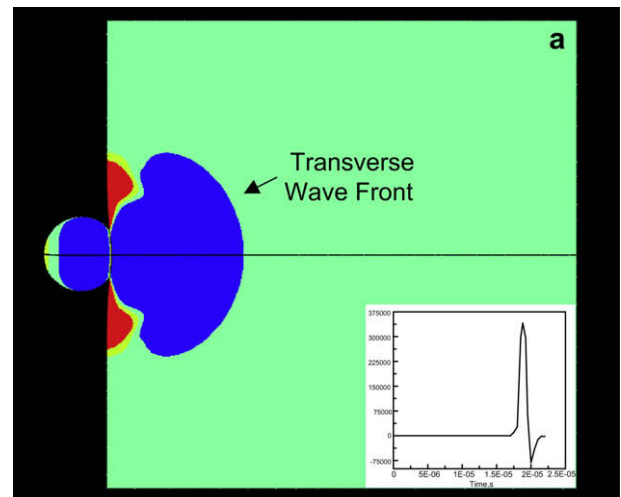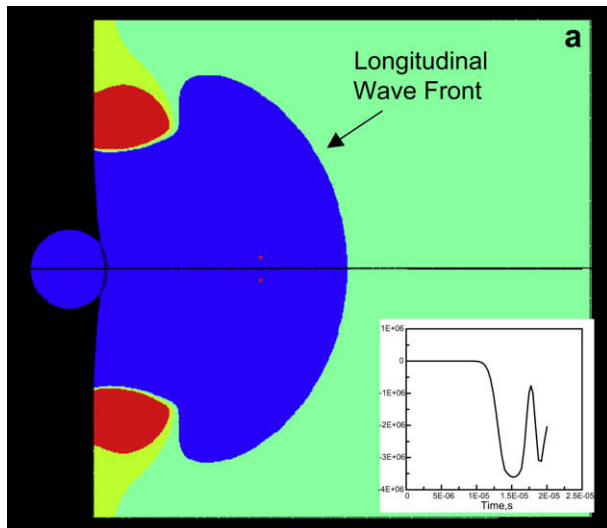

Fig. 5. A comparison of the longitudinal stress-wave fronts obtained (a) computationally and (b) experimentally (in Refs. [3,4]) for the case of a spherical impactor with an initial velocity of 440 m/s and a post-impact time of 7.7 μs. The inset in (a) shows a typical longitudinal-wave trace.

Fig. 6. A comparison of the transverse stress-wave fronts obtained (a) computationally and (b) experimentally (in Refs. [3,4]) for the case of a spherical impactor with an initial velocity of 440 m/s and a post-impact time of 7.7 μs. The inset in (a) shows a typical transverse-wave trace.

value of shear stress which can be transmitted before the contacting surfaces begin to slide).

The impact of the projectile with the target is modeled by assigning an initial (translational) velocity to the projectile ("*the initial condition*"). The initial velocity of the target was set to zero and, during the impact simulation, the narrow side face of the target normal to the impacted face was kept at a fixed position ("*the boundary conditions*").

To prevent hour-glassing effects which may arise due to the use of reduced-integration elements, a default value of hour-glass stiffness was used. No mass-scaling algorithm was used to increase the maximum stable time increment. Computational analyses were run on a machine with two 2.33 GHz Quad-core Intel Xeon processors with 16 GB of RAM. A typical 20 μs impactor/target computational analysis would require 20 min of (wall-clock) time.

4. Results and discussion

In Section 3.2, a detailed description was provided regarding the transient non-linear dynamics finite element analyses of the EOI tests of plate-like soda-lime glass targets with either a spherical or a cylindrical projectile. In the present section, the main results of the EOI computational analyses are presented and discussed.

4.1. Propagation of longitudinal and transverse stress waves

To verify that the pre-damage initiation elastic portion of the material model for soda-lime glass was implemented correctly into the VUMAT User Material Subroutine and correctly linked with the ABAQUS/Explicit finite-element solver, the propagation of the (elastic) longitudinal stress waves and transverse stress waves were investigated first. The contour plots displayed in Figs. 5(a) and 6(a) show respectively the positions of the longitudinal and transverse stress-wave fronts 7.7 μs after the impact with the spherical projectile (propelled with an initial velocity of 440 m/s). For comparison, the corresponding results obtained experimentally in Ref. [3] (using a cross-polarization photo-elastic experimental technique), are shown in Figs. 5(b) and 6(b), respectively. It is evident that both the computed shape of the stress-wave fronts and their locations are in fairly good agreement with their experimental counterparts. The same conclusion is reached after analyzing the results displayed in Figs. 7(a) and (b) and 8(a) and (b). In these figures, a comparison is made between the computed and experimental results pertaining to the position of the longitudinal and transverse stress-wave fronts 15.7 μs after the impact
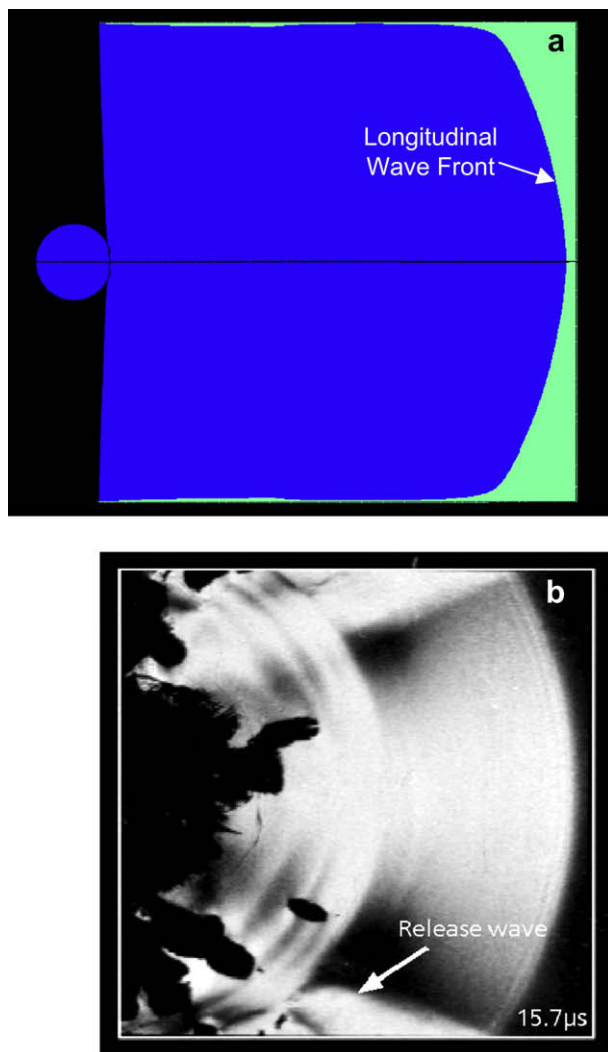

Fig. 7. A comparison of the longitudinal stress-wave fronts obtained (a) computationally and (b) experimentally (in Refs. [3,4]) for the case of a spherical impactor with an initial velocity of 440 m/s and a post-impact time of 15.7 μs.

Fig. 8. A comparison of the transverse stress-wave fronts obtained (a) computationally and (b) experimentally (in Refs. [3,4]) for the case of a spherical impactor with an initial velocity of 440 m/s and a post-impact time of 15.7 μs.
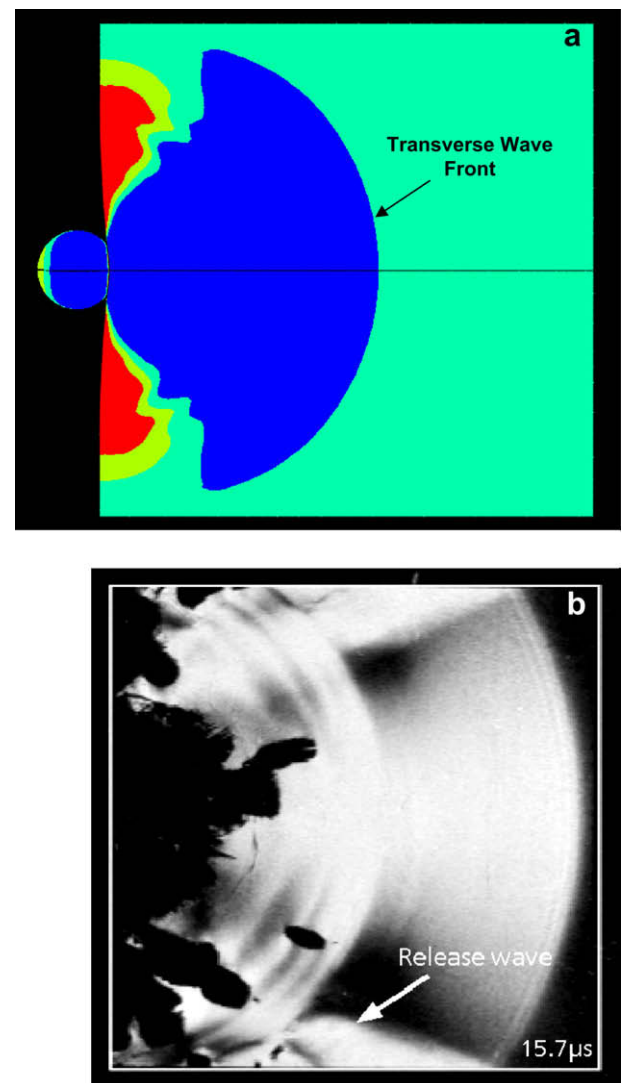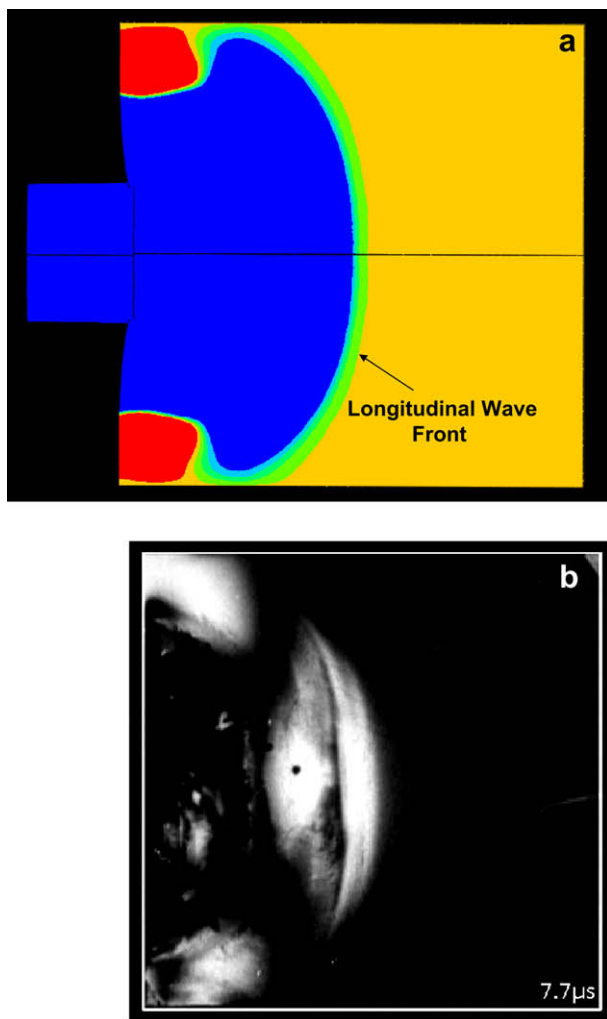
Fig. 9. A comparison of the longitudinal-wave fronts obtained (a) computationally and (b) experimentally (in Refs. [3,4]) for the case of a cylindrical impactor with an initial velocity of 390 m/s and a post-impact time of 7.7 μs.

Fig. 10. A comparison of the transverse-wave fronts obtained (a) computationally and (b) experimentally (in Refs. [3,4]) for the case of a cylindrical impactor with an initial velocity of 390 m/s and a post-impact time of 7.7 μs.

with the same spherical projectile propelled with the same initial velocity.

A similar comparison is made in Figs. 9–12 for the case of the cylindrical impactor (propelled with an initial velocity of 390 m/s) at post-impact times of 7.7 μs and 15.7 μs. Again it is found that both the computed shape of the stress-wave fronts and their locations are in fairly good agreement with their experimental counterparts.

To further validate the implementation of the elastic part of the material model, a number of gage points were placed along the centerline of the target (in the direction of propagation of projectile motion) and the moment of arrival of the longitudinal and transverse stress-wave fronts recorded. Typical stress vs. time traces obtained are shown (as insets) in Figs. 5(a) and 6(a). From the distances between the gage points and the time-of-arrival of the stress waves to the gage points, the average longitudinal and transverse stress-wave velocities were obtained as $v_{\text{long}} = 5890 \pm 100$ m/s and $v_{\text{trane}} = 3410 \pm 70$ m/s. These results are in quite good agreement with their experimental counterparts (5763 m/s and 3518 m/s) and the ones obtained by using the Young's and shear moduli and the material density (5407 m/s and 3413 m/s), respectively.

Based on the results obtained and discussed in this section, it can be concluded that the elastic portion of the soda-lime glass material model is appropriate.
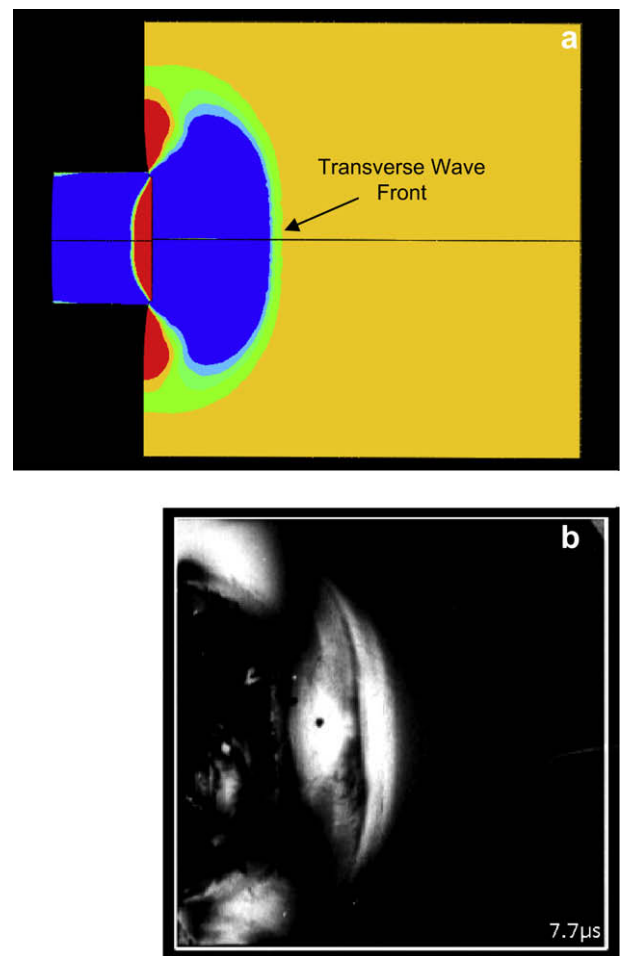
4.2. Temporal evolution of the coherent-damage/comminution zone

As discussed in Section 3.1, the region surrounding the target face impacted by the projectile suffers damage (and ultimately fine-fragmentation fracture) due to formation of the micron- and sub-micron-size cracks. The extent of this "*coherent*" damage at a given material point is represented in the present work by a scalar material state variable, *D*. While in many brittle-fracture material models existing in the literature damage is represented using a tensorial quantity (in order to account for the anisotropic nature of the damage), the extent of such anisotropy within the coherent-damage zone is generally quite small. Although the extent of damage experienced by individual elements was found, in the present work, to be affected by the choice of the isotropic damage model, the overall size and shape of the coherent-damage zones were found not to be significantly changed when damage was treated as an anisotropic phenomenon. Consequently and considering the fact that the computational cost was more than doubled, the use of a damage tensor was deemed unwarranted.

To test the ability of the present material model for soda-lime glass to account for the temporal evolution of size and shape of the coherent-damage zone, a series of comparisons is made in Figs. 13–16 between the computational results pertaining to size and shape of the coherent-damage zone (obtained in the present work) and their experimental counterparts (obtained in the shadow-graph technique in Refs. [3,4]). In Figs. 13–16, part (a) contains the
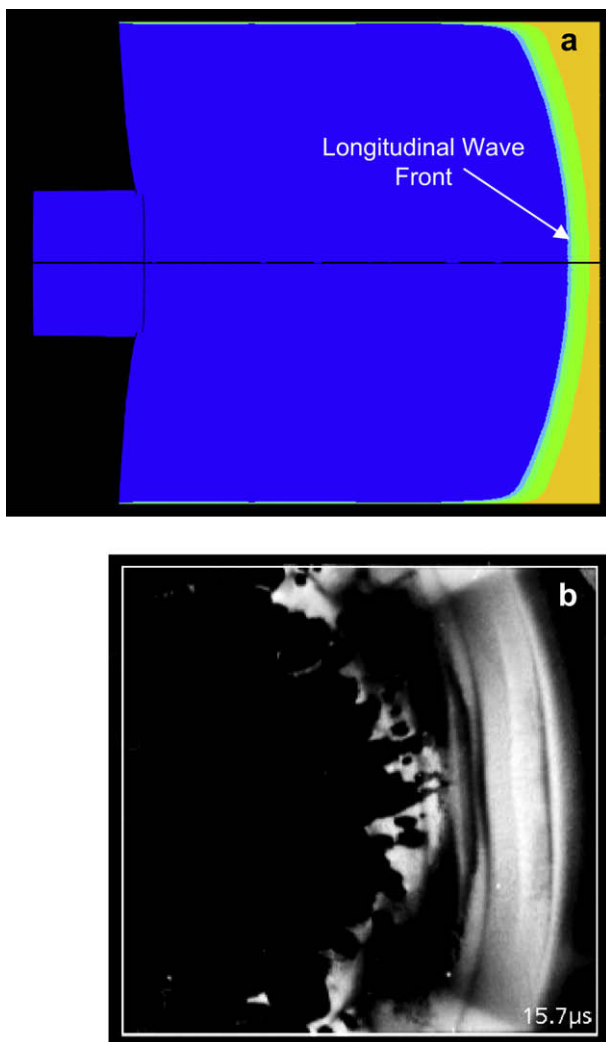
Fig. 11. A comparison of the longitudinal-wave fronts obtained (a) computationally and (b) experimentally (in Refs. [3,4]) for the case of a cylindrical impactor with an initial velocity of 390 m/s and a post-impact time of 15.7 μs.

Fig. 12. A comparison of the transverse-wave fronts obtained (a) computationally and (b) experimentally (in Refs. [3,4]) for the case of a cylindrical impactor with an initial velocity of 390 m/s and a post-impact time of 15.7 μs.

computational results while part (b) contains the corresponding experimental results.

The results displayed in Figs. 13 and 14 pertain to the case of a spherical projectile (the initial velocity = 440 m/s and the post-impact times of 7.7 μs and 15.7 μs, respectively), while the results displayed in Figs. 15 and 16 correspond to the case of a cylindrical projectile (the initial velocity = 390 m/s and the post-impact times of 7.7 μs and 15.7 μs, respectively). While the computational results can reveal detailed spatial distribution of damage within the coherent-damage zone, similar details cannot be obtained using the shadow-graph technique. Consequently, only the size and the shape of the coherent-damage zones are used for comparison of the computational and the experimental results.

A careful examination of the results displayed in Figs. 13–16 shows that: (a) there is a reasonably good agreement between the computational and the experimental results pertaining to both size and shape of the coherent-damage zone both at shorter (e.g. 7.7 μs) post-impact times (Figs. 13 and 15) and at longer (e.g. 15.7 μs) post-impact times (Figs. 14 and 16); (b) there is also a reasonably good agreement between the computational and the experimental results pertaining to the extent of coherent-damage zone along the target face impacted by the projectile, both at shorter and longer post-impact times. The extent of coherent-damage zone along the
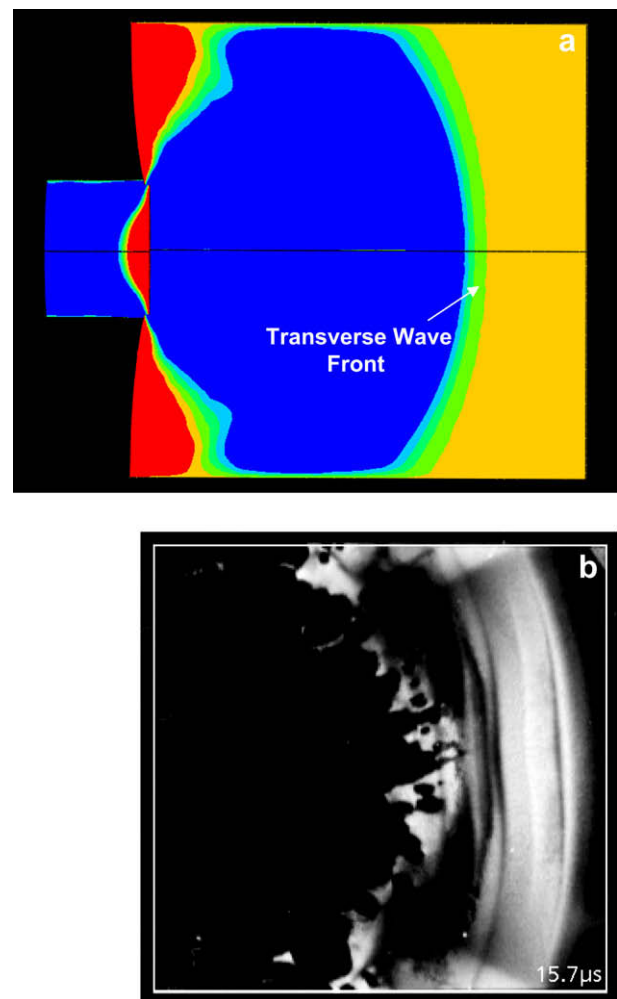
target face impacted by the projectile is controlled by surface flaws while the evolution of damage in the remainder of the zone is controlled by bulk flaws; and (c) the computed depth of the coherent-damage zone along the target face impacted by the projectile is significantly smaller than the one observed experimentally (e.g. Fig. 14(a) and (b)); and (d) the onset of damage along the (top and bottom) clamped faces of the target is under-predicted (e.g. Fig. 14(a) and (b)).

There are several potential reasons for the aforementioned discrepancies. Two most likely reasons are (a) the fixtures used to hold the target during impact introduce stresses into the target which, when superposed with the impact-induced stresses, can cause an early damage initiation in the regions near the target top and bottom surfaces; and (b) cutting and grinding of the side faces of the target used during the target manufacturing process may have changed the distribution and potency of surface flaws relative to those corresponding to the surface-flaw Weibull distribution parameters listed in Table 1. Both of the aforementioned hypotheses were tested in the present work. The first one was tested by adding compressive-normal and shear tractions to the top and bottom target faces while the second hypothesis was investigated by reducing the mean fracture strength for the finite elements which reside on the impacted and top and bottom clamped faces of the target. The results obtained (not shown for brevity) suggest that both of the hypothesized reasons may account for the observed
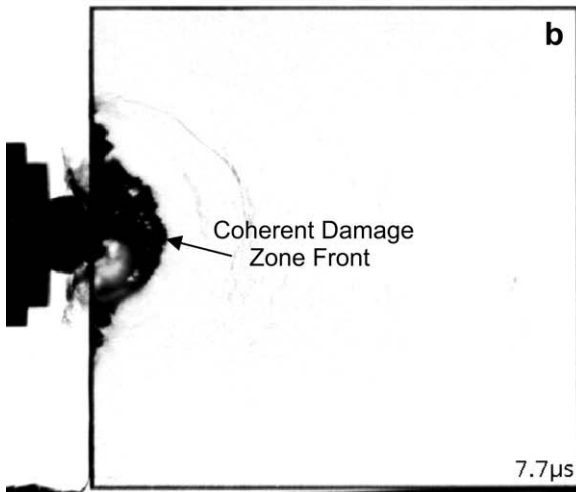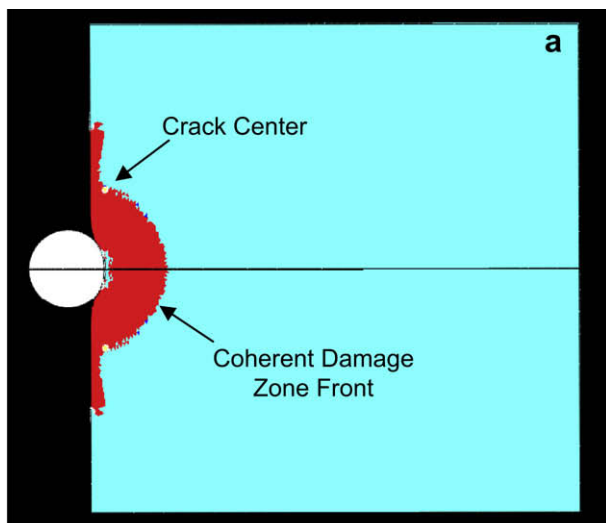
Fig. 13. A comparison of the coherent-damage zone fronts obtained (a) computationally and (b) experimentally (in Refs. [3,4]) for the case of a spherical impactor with an initial velocity of 440 m/s and a post-impact time of 7.7 μs.

Fig. 14. A comparison of the coherent-damage zone fronts obtained (a) computationally and (b) experimentally (in Refs. [3,4]) for the case of a spherical impactor with an initial velocity of 440 m/s and a post-impact time of 15.7 μs.

discrepancy between the computed and experimental shapes of the continuum-damage zones. Thus, additional experimental investigation is needed to help resolve this uncertainty. Such experimental investigation may involve the use of chemical polishing which may reduce considerably the amount of damage induced by cutting/grinding.

To summarize, based on the results presented in this section, it appears that the proposed material model for soda-lime glass can capture the essential features of the temporal evolution of the coherent-damage zone. It is also found that more experimental work is needed to establish if target-fixturing or cutting/grinding-induced surface flaws alter the stress/microstructural state of the surface regions. Either of these effects can be readily included as fixturing-induced loads (i.e. through the changes in boundary conditions) or through changes in the values of the surface-flaw Weibull distribution parameters used in the present material model for soda-lime glass.

4.3. Temporal evolution of the discrete damage

As discussed earlier, the experimental investigations carried out by Strassburger et al. [3,4] revealed the formation of discrete da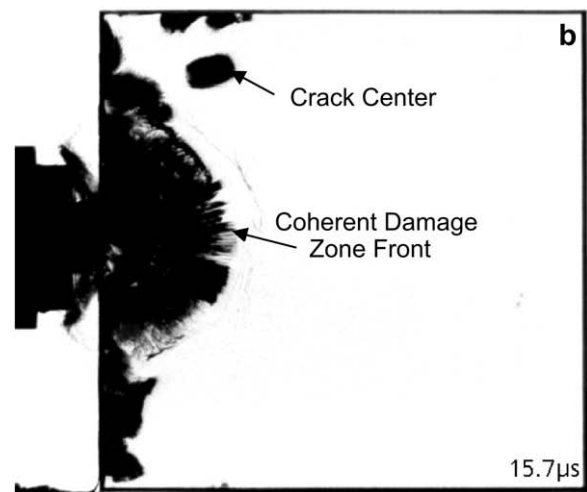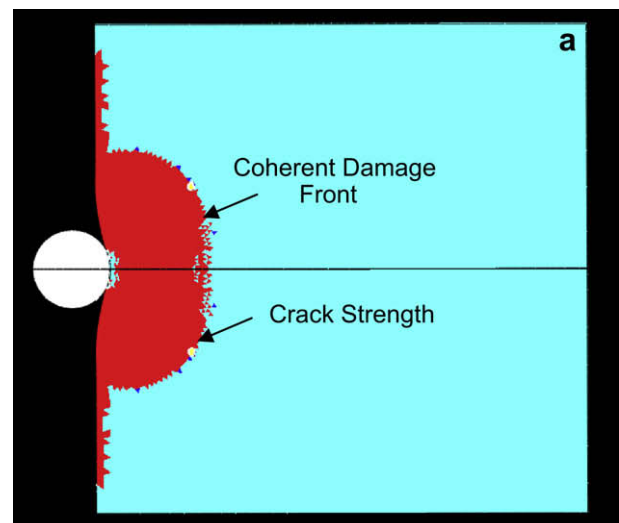mage (i.e. "*crack centers*") at a small distance ahead of the advancing coherent-damage zone front. To allow for the formation of discrete cracks, as discussed in Section 2.3, a stress-rate based criterion was used to control the mode of damage and ultimate failure of the soda-lime glass under impact loading conditions. That is, at stress rates lower that a critical stress-rate, the material point within a finite element at which the stress-based condition for the onset of damage is satisfied, is assigned a "*static-type*" coarse-fragmentation failure mode to reflect the fact that the first crack to form in such an element would traverse the entire element before additional cracks can nucleate. Conversely, material points residing within the finite elements which reach the stress-based damage-initiation condition at high stress rates are assumed to undergo coherent damage and to fail in a "*dynamic-type*" multiple-fragmentation mode. This was justified by the fact that at high stress rates and the associated high stress levels, the criterion for crack nucleation is met at many points within the element.

The results obtained in the present work, Figs. 13(a)–16(a) revealed the presence of finite elements that failed in the coarse-fragmentation mode (labeled as "*crack centers*"). It should be noted that, the present model is capable of modeling the nucleation and propagation of discrete cracks only within individual elements and not crack propagation across boundaries of
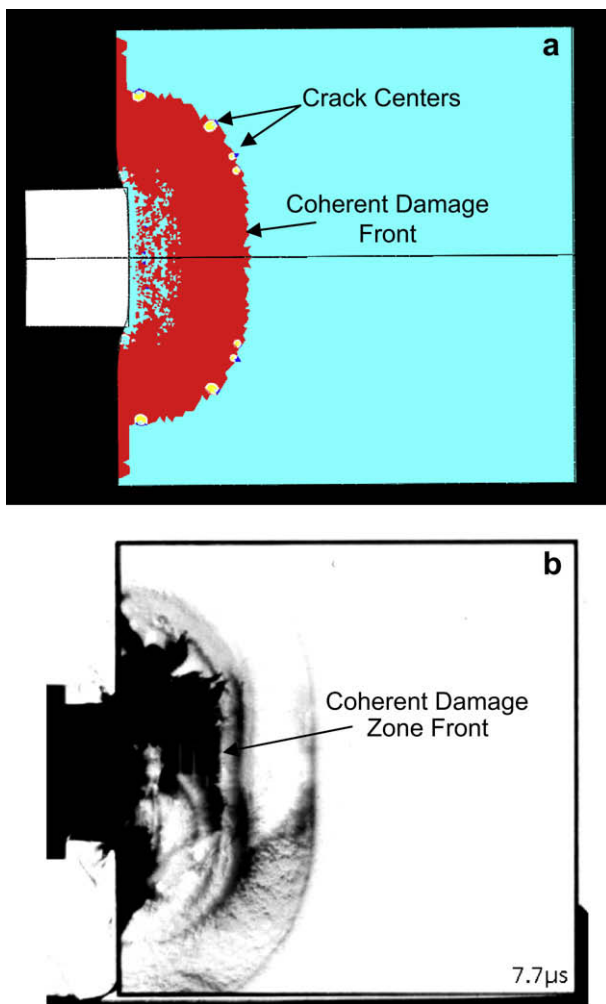
Fig. 15. A comparison of the coherent-damage zone fronts obtained (a) computationally and (b) experimentally (in Refs. [3,4]) for the case of a cylindrical impactor with an initial velocity of 390 m/s and a post-impact time of 7.7 μs.
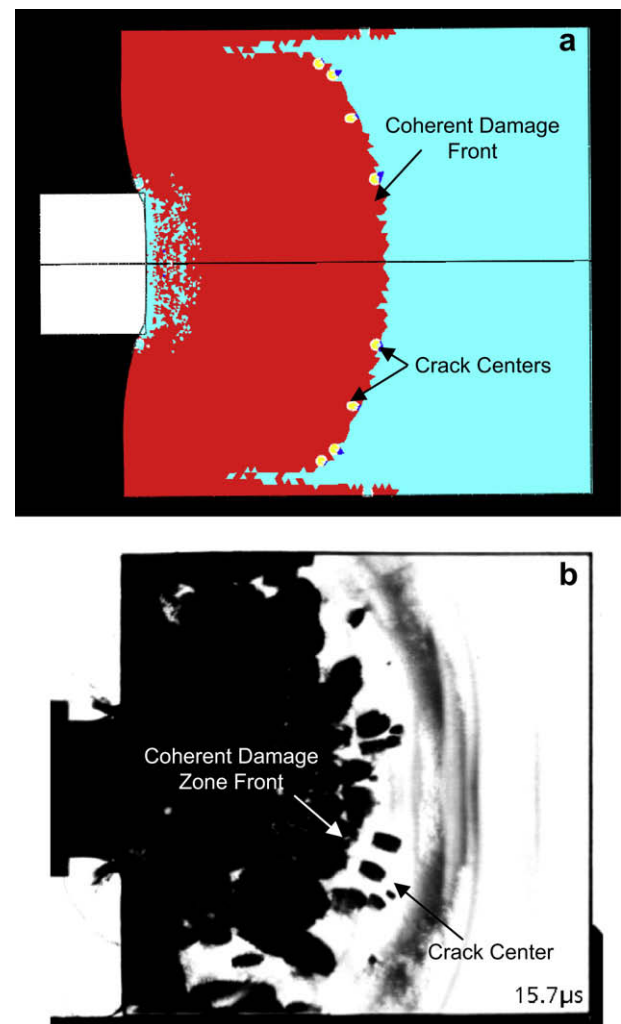

Fig. 16. A comparison of the coherent-damage zone fronts obtained (a) computationally and (b) experimentally (in Refs. [3,4]) for the case of a cylindrical impactor with an initial velocity of 390 m/s and a post-impact time of 15.7 μs.

the adjacent elements. Modeling the latter "*Meso-scale*" damage phenomenon can be done using a stress-intensity factor-based approach [20]. This was not done in the present work due to the following two reasons: (a) difficulties encountered during implementation of this "*Non-local*" approach into a commercial finite-element program; and (b) due to the substantially increased computational cost.

These elements were nucleated essentially at the front of the coherent damage zone. While the experimental findings of Strassburger et al. [3,4] suggested that isolated cracks form at a short distance ahead of the coherent-damage zone front, it must be noted that the experimental technique employed by Strassburger et al. [3,4] had serious limitations concerning the discrimination between the two modes of damage. Consequently, the predictions made by the current material model for soda-lime glass regarding the formation of discrete cracks can be considered as encouraging. It should be also noted that the results obtained in the present work suggest that the evolution of shape and size of the coherent-damage zone is not significantly affected by the formation of the discrete cracks. Also, discrete cracks were not found to significantly affect the ability of the glass to absorb the kinetic energy of the projectile. While this finding is important from the standpoint of the present material model to accurately predict the (single- and multiple-

hit) ballistic-protection capacity of soda-lime glass (which is the subject of our current work), the presence of discrete cracks (particularly if they are located at a distance from the coherent-damage zone front, as observed by Strassburger et al. [3,4]) can compromise transparency of glass (a critical performance factor for transparent armor).

4.4. Computational efficiency of the material model

As discussed earlier, the main objective of the present work was to develop a simple, physically based, high strain-rate, high-pressure, large-strain constitutive model for soda-lime glass suitable for direct incorporation into standard commercial transient non-linear dynamics finite-element based software packages and computationally efficient so that it can be used in large-scale simulations of the multi-hit ballistic performance of multi-layer functional transparent-armor systems. In our recent work [18], a new two length-scale material model for soda-lime glass was proposed. Within this model, solid finite elements and a linear-elastic degradable material model was used to simulate the evolution of the coherent damage while interfacial ("*cohesive*") elements and a traction-separation material law was used to model the evolution of discrete cracks. The model developed

in Ref. [18] was also validated against the EOI experimental results of Strassburger et al. [3,4]. A comparison of the predictions of the two material models for soda-lime glass with their experimental counterparts from Refs. [3,4] shows that the material model developed in the present work is in better agreement with the experiment and that it is computationally faster by a factor of 5–6 than the material model developed in Ref. [18].

5. Summary and conclusions

Based on the material model development procedure utilized and the results of the subsequent computational analyses, the following main summary remarks and conclusions can be drawn:

1. Material property data and various experimental observations reported in the open literature and the multiple-fragmentation fracture model proposed by Denoual and Hild [13,19] are used to construct a computationally efficient ballistic material model for soda-lime glass.
2. To test the model, a series of transient non-linear dynamics analyses pertaining to the edge-on-impact of plate-like soda-lime glass targets with either a spherical or cylindrical projectile was conducted and the results obtained compared with their experimental counterparts as reported by Strassburger et al. [3,4].
3. A comparison between the computed and experimental results revealed that the proposed model fairly well accounts for the propagation of the elastic (longitudinal and transverse) waves in the target following impact and that the predicted speeds of these waves are quite comparable with their experimental counterparts.
4. Likewise, a good agreement between the computed and experimental results is obtained relative to the temporal evolution of size and the shape of the coherent-damage zone (i.e. the zone surrounding the projectile/target contact surface which contains a large number of fine cracks).
5. Minor computation/experiment discrepancies were observed relative to the extent of damage along the cut/ground and clamped narrow faces of the soda-lime glass target and these were respectively attributed to the cutting/grinding-induced flaws and the target-fixturing-induced stresses.
6. The model was also capable of accounting (at least qualitatively) for the observed formation of localized damage (i.e. crack centers) ahead of the advancing coherent-zone front.

Acknowledgements

Appendix. Quasi-static vs. dynamic failure regimes

A.1. Course-fragmentation quasi-static failure regime

Under low-rate (i.e. quasi-static) loading conditions, a coarse-fragmentation failure regime is typically observed in which the failure of the complete structure is caused by the nucleation and propagation of a single crack or few cracks. Under low-deformation rates, stresses are increasing slowly within the material. When the stresses become high enough, the first crack nucleates and begins to propagate at a terminal crack velocity. As the crack grows so does

the zone around it within which stresses are relaxed ("*the shielding zone*") and all defects located within the shielding zone becomes impotent. Due to a low rate of stress increase in the remainder of the material, the stresses typically never reach a critical level needed to nucleate many additional cracks and, consequently, the coarse-fragmentation regime ensues. Under such conditions, the fracture strength of the brittle material behaves as a stochastic quantity, i.e. the fracture resistance of a brittle material is not defined using a single (mean value) fracture strength, but rather by a failure probability function. To derive an expression for the failure probability, the coarse-fragmentation fracture regime is analyzed using a Poisson point-process framework. Within this framework, the probability P of finding $N = B$ crack-nucleating defects within a uniformly loaded domain Z is expressed in terms of a Poisson distribution function as:

$$P(N = B) = \frac{[\lambda_t(\sigma)Z]^B}{B!} \exp[-\lambda_t(\sigma)Z] \tag{A.1}$$

The product $\lambda_t(\sigma)Z$ in Eq. (A.1) corresponds to the average number of crack-nucleating defects at the uniformly applied stress σ within a domain Z (a volume, for volume-flaw controlled fracture and a surface area, for surface-flaw controlled fracture). The (Weibull) failure probability P_F is then defined as the probability of finding at least one crack-nucleating defect in the domain Z as:

$$P_F = P(N \geq 1) = 1 - P(N = 0) = 1 - \exp[\lambda_t Z] \tag{A.2}$$

The stress-dependence of λ_t is defined within the Weibull fracture framework as:

$$\lambda_t = \lambda_0 \left(\frac{\sigma}{S_0}\right)^m \tag{A.3}$$

where λ_0 and S_0 are the reference density and a stress normalizing parameter, while the exponent m is generally referred to as the Weibull modulus.

Using standard expressions for the mean value and the standard deviation, the mean static fracture strength and its standard deviation for a brittle material can be defined as:

$$\sigma_{f,\text{static}} = \frac{S}{\left(Z_{\text{eff}}\lambda_0\right)^{1/m}} \Gamma\left(1 + \frac{1}{m}\right) \tag{A.4}$$

$$\sigma_{\text{sd}} = \sqrt{\frac{S_0^2}{\left(Z_{\text{eff}}\lambda_0\right)^{2/m}} \Gamma\left(1 + \frac{2}{m}\right) - \sigma_{f,\text{static}}^2} \tag{A.5}$$

where Γ denotes the gamma function which is defined as:

$$\Gamma(x) = (x - 1)! \tag{A.6}$$

where the probability distribution function for the fracture strength is obtained by combining Eqs. (A.2) and (A.3) and differentiating the resulting equation with respect to σ.

A.2. Multiple fine-fragmentation/comminution dynamic failure regime

Under high-rate (i.e. dynamic) loading conditions, it is generally observed that damage and the final failure occurs by nucleation, growth and interconnection of multiple micron- and millimeter-size cracks. In the following, a brief overview is provided of the dynamic multiple-fragmentation fracture model proposed by Denoual and Hild [13,19], the model whose physical concepts were

used in the present work. The model of Denoual and Hild [13,19] is based on the following approximations and simplifying assumptions:

(a) When a defect is activated and the associated crack is nucleated, a shielding zone is created around the crack within which stress component responsible for crack nucleation is relaxed to zero. Consequently, any defect residing in such a zone will become impotent (i.e. will no longer represents the potential nucleus for a crack). As a crack grows, its shielding zone also grows but in a self-similar fashion. The size of the shielding zone at a time t associated with a crack which was nucleated at the time τ is defined by the following relation:

$$Z_{\text{sh}}(t,\tau) = S[kC(t - \tau)]^n \tag{A.7}$$

where $C = [E/\rho]^{0.5}$ is the speed of sound (i.e. the speed of the impact-generated stress wave), E the Young's modulus, ρ the mass density, $k = 0.2$–0.4, a ratio of the crack speed and the sound speed, n a defect-distribution dimensionality factor ($=2$, for surface-flaw dominated failure and $=3$, for bulk flaw dominated failure) and S is a shielding zone shape factor ($= 4\pi/3$, for a spherically shaped bulk shielding zone);

(b) Under quasi-static loading conditions, once a crack is nucleated, it can traverse the entire structure (while it's shielding zone spreads over the entire surface/volume of the structure) before the stress on other defects can become sufficiently high to cause the nucleation of additional cracks. Under dynamic loading, on the other hand, the condition for crack nucleation will be met at many flaws leading to a multiple-cracking fracture mode. However, the neighboring cracks with compatible opening modes and orientations, via their shielding zone, will mutually terminate each other's growth, giving rise to relatively short cracks;

(c) Due to the shielding effects discussed above, one can distinguish between the non-shielded and shielded defects and the total defect density can be decomposed as:

$$\lambda_t = \lambda_{\text{non-sh}} + \lambda_{\text{sh}} \tag{A.8}$$

It should be noted that both $\lambda_{\text{non-sh}}$ and λ_{sh} are defined by dividing the corresponding number of defects by the total domain size;

(d) The extent of defect shielding is controlled by the competition between the expansion of the shielding zone(s) (which promote defect shielding) and higher rates of loading (which promote activation of new defects in the regions outside the shielding zones). As the rate of loading is decreased, a larger number of defects will become shielded and, in the limit of quasi-static loading, all defects (except for the one which nucleated the first crack) will be shielded leading to the coarse-fragmentation failure mode; and

(e) As the loading rate increases, the density of shielded defects will decrease (at a given level of stress, i.e. at a given level of total defect density). This, in turn, will give rise to higher fracture-strength levels, as a larger portion of the domain will remain unshielded (i.e. undamaged) and could support the applied load.

To explain the essential analytical features of the multiple-fragmentation brittle-fracture model proposed by Denoual and Hild [13,19], the case of uniform loading at a constant stress rate is considered, $\dot{\sigma}$. At this point, one must distinguish between the externally applied macroscopic stress, Σ and an internal stress

$\sigma = \dot{\sigma}t$, where t is the time of loading. Due to the formation of cracks and their shielding zone (within which the internal stress is relaxed), only non-shielded portions of the brittle-material structure can support σ. If a damage variable, D, is defined as a ratio of the union of all shielding-zone volumes and the structure volume, then the following relations exist between Σ and σ:

$$\Sigma = \sigma(t)(1 - D(\sigma)) = \dot{\sigma}t(1 - D(\dot{\sigma}, t)) \tag{A.9}$$

where D is implied to depend on $\dot{\sigma}$ and t, since these quantities affect the density/number of cracks via $\sigma = \dot{\sigma}t$ and Eq. (A.3) while t affects the size of the shielding zones via Eq. (A.7).

According to Eq. (A.9), as the loading time increases, the $\sigma(t)$ increases while the $(1 - D(\sigma))$ term decreases. The macroscopic multiple-fragmentation fracture strength is then defined as the peak value of Σ, i.e. $\sigma_{f,\text{dynamic}} = \Sigma_{\max}$, and is obtained from the relation:

$$\frac{\text{d}\Sigma}{\text{d}\sigma} = 0 \tag{A.10}$$

The basic assumption in the multiple-fragmentation brittle-fracture model of Denoual and Hild [13,19] is that D is equal to the probability of defect shielding, P_{sh}, which is then defined using Eq. (A.2) as:

$$D = P_{\text{sh}} = 1 - \exp(-\lambda_t Z_{\text{sh}}) \tag{A.11}$$

where Z_{sh} is the average size of the shielding zone defined as:

$$\lambda_t(t)Z_{\text{sh}}(t) = \int_0^t \frac{\text{d}\lambda_t}{\text{d}t}\bigg|_\tau [kC(t - \tau)]^n \text{d}\tau \tag{A.12}$$

Eq. (A.12) states that, in order to compute Z_{sh} at time t, when the total defect density is $\lambda_t(t)$, one must take into account that cracks may have nucleated at a time, $0 \le \tau \le t$, and that their shielding-zone size is, hence, $[kC(t - \tau)]^n$. Furthermore, the probability that a crack present at time t was nucleated at time τ is expected to be proportional to the rate of activation of the flaws at time τ, i.e. to scale with $1/\lambda_t(t)\text{d}\lambda_t/\text{d}t|_\tau$ (it should be also noted that $\int_0^t \lambda_t(t)\text{d}\lambda_t/\text{d}t|_\tau^n \text{d}\tau = 1$).

In the case of uniform loading under constant stress-rate conditions, the term $\text{d}\lambda_t/\text{d}t|_\tau$ becomes via Eq. (A.3):

$$\frac{\text{d}\lambda_t}{\text{d}t}\bigg| = \frac{\lambda_0 m\dot{\sigma}^m t^{m-1}}{S_0^m} \tag{A.13}$$

When Eq. (A.13) is substituted into Eq. (A.12) and, in turn, in Eq. (A.11), and integrated, the following expression is obtained:

$$D = 1 - \exp\left(-\frac{m!n!(\frac{\sigma}{\sigma_c})^{m+n}}{(m + n)!}\right) \tag{A.14}$$

where σ_c is a characteristic stress defined below.

To derive an expression for σ_c, the following normalized quantities are introduced:

$$\bar{\lambda} = \frac{\lambda}{\lambda_c}, \quad \bar{t} = \frac{t}{t_c}, \quad \bar{Z}_{\text{sh}} = \frac{Z_{\text{sh}}}{Z_c} \quad \text{and} \quad \bar{\sigma} = \frac{\sigma}{\sigma_c}$$

where the characteristic quantities (denoted by the subscript "c") are defined from the condition:

$$\lambda_{t,c}Z_{\text{sh,c}} = \lambda_t(t = t_c)Z_{\text{sh}}(t = t_c, \tau = 0) = 1 \tag{A.15}$$

where λ_t and Z_{sh} are given by Eqs. (A.3) and (A.7), respectively. The characteristic quantities are stress-rate dependent and correspond

to the condition during loading when a single shielding zone (created at time $\tau = 0$) has grown to the size which is large enough to cause shielding of at least one defect.

By combining Eqs. (A.3), (A.7) and (A.15) and setting $\sigma = \dot{\sigma}t$, one obtains:

$$t_{\mathrm{c}} = \left[\frac{S_0^m}{\lambda_0 S(kC)^n \dot{\sigma}^m}\right]^{\frac{1}{m+n}} \tag{A.16}$$

After substitution of Eq. (A.16) into Eq. (A.7), the following relation is obtained:

$$Z_{\mathrm{c}} = \left[\frac{(S_0 kC)^m S^{\frac{m}{n}}}{\lambda_0 \dot{\sigma}^m}\right]^{\frac{n}{m+n}} \tag{A.17}$$

Likewise, after substitution of Eq. (A.16) into Eq. (A.3), one obtains:

$$\lambda_{\mathrm{c}} = \left[\frac{\lambda_0 \dot{\sigma}^m}{S_0 S^{m/n}(kC)^m}\right]^{\frac{n}{m+n}} \tag{A.18}$$

Furthermore:

$$\sigma_{\mathrm{c}} = \dot{\sigma}t_{\mathrm{c}} = \left[\frac{S_0^m \dot{\sigma}^n}{\lambda_0 S(kC)^n}\right]^{\frac{1}{m+n}} \tag{A.19}$$

After substituting Eq. (A.14) into Eq. (A.19) and after differentiating the resulting equation in accordance with Eq. (A.10) one obtains:

$$\sigma|_{\Sigma_{\max}} = \left(\frac{S_0^m \dot{\sigma}^n}{\lambda_0 S(kC)^n}\right)^{\frac{1}{m+n}} \left(\frac{(m+n-1)!}{m!n!}\right)^{\frac{1}{m+n}} \tag{A.20}$$

$$\sigma_{f,\mathrm{dynamic}} = \Sigma_{\max} = \sigma_{\mathrm{c}} \left[\frac{1}{e}\frac{(m+n-1)!}{m!n!}\right]^{\frac{1}{m+n}} \tag{A.21}$$

Then Eqs. (A.20) and (A.14) are combined to get:

$$D|_{\Sigma_{\max}} = 1 - \left(\frac{1}{e}\right)^{\frac{1}{m+n}} \tag{A.22}$$

Likewise, $\sigma = \dot{\sigma}t$ and Eq. (A.20) are combined to get:

$$t|_{\Sigma_{\max}} = \left(\frac{S_0^m}{\lambda_0 S(kC)^n \dot{\sigma}^m}\right)^{\frac{1}{m+n}} \left(\frac{(m+n-1)!}{m!n!}\right)^{\frac{1}{m+n}} \tag{A.23}$$

To demonstrate the relationship between the two expressions for the fracture strength, i.e. between Eqs. (A.4) and (A.21), a fracture strength vs. stress-rate plot is displayed in Fig. A1 for soda-lime glass for the case when brittle fracture is controlled by bulk flaws. The relevant mechanical property parameters are listed in Table 1. To help interpret the results displayed in Fig. A1, a second horizontal axis, $Z_{\mathrm{eff}}/Z_{\mathrm{c}}$, is introduced. It should be noted that the results displayed in Fig. A1 correspond to a fixed value of $Z_{\mathrm{eff}} = 10^{-4}$ m^3. When analyzing the results displayed in Fig. A1, one must note that the two expressions for the (mean) fracture strength, Eqs. (A.4) and (A.21), are valid only over a limited range of stress rates and that the ranges are different for the two relations. That is, at high stress rates, defect shielding is limited and, hence, the static course-fragmentation fracture strength relation, Eq. (A.4), which assumes complete shielding of all flaws by the first nucleated crack is not valid. Likewise, Eq. (A.23) is not valid in the low stress rate range (i.e. at lower values of $Z_{\mathrm{eff}}/Z_{\mathrm{c}}$), since in this case, a shielding zone must grow beyond the total structure volume before a single defect

is shielded. Thus the multiple-cracking fracture mode is not feasible. The results displayed in Fig. A1 further show that, as expected, the fracture strength increases with an increase in stress rate in the multiple-fragmentation regime at high stress rates, while it is essentially stress-rate independent in the single-fragmentation fracture mode at low stress rates.
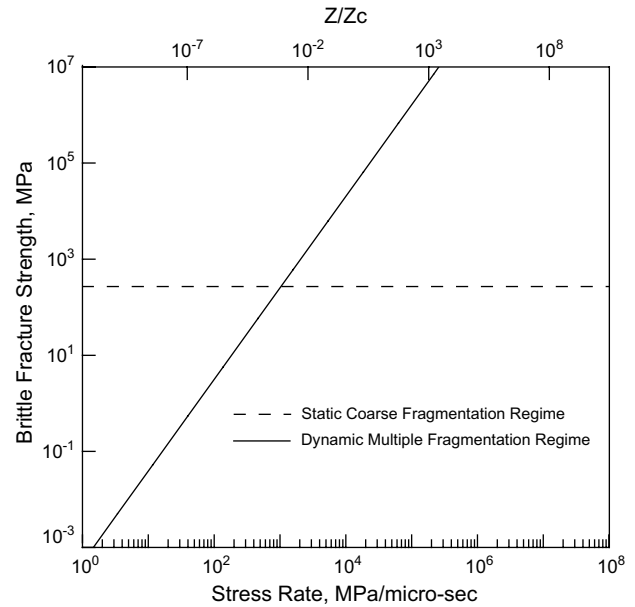

Fig. A1. The transition between the static coarse-fragmentation and the dynamic fine-fragmentation brittle-fracture modes as a function of an increase in stress-rate.

References

[1] ANSYS/Autodyn version 11.0, User documentation, Century Dynamics Inc. a subsidiary of ANSYS Inc.; 2007.
[2] ABAQUS version 6.7, User documentation, Dessault systems, 2007.
[3] Strassburger E, Patel P, McCauley JW, Kovalchick C, Ramesh KT, Templeton DW. High-speed transmission shadowgraphic and dynamic photoelasticity study of stress wave and impact damage propagation in transparent materials and laminates using the edge-on impact method. In: Proceedings of the twenty-third international symposium on ballistics. Spain: April 2007.
[4] Strassburger E, Patel P, McCauley W, Templeton DW. Visualization of wave propagation and impact damage in a polycrystalline transparent ceramic-AlON. In: Proceedings of the twenty-second international symposium on ballistics. Vancouver, Canada: November 2005.
[5] AMPTIAC quarterly: army materials research: transforming land combat through new technologies, 8, no.4, 2004.
[6] Sun DZ, Andreiux F, Ockewitz A. Modeling of the failure behavior of windscreens and component tests. In: Fourth LS-DYNA users' conference. Bamberg, Germany: 2005.
[7] Zarzycky T. Glasses and the vitreous state. Cambridge, UK: Cambridge University; 1991.
[8] B Nghiem. Ph.D. thesis, University of Paris 6, France; 1998.
[9] Brajer X, Forquin P, Rene G, Hild F. The role of surface and volume defects in the fracture of glass under quasi-static and dynamic loadings. Journal of Non-Crystalline Solids 2003;316:42–53.
[10] Guillemet C. In: Kurkjian CR, editor. Strength of inorganic glass. New York: Plenum; 1985. p. 1–26.
[11] Gy R, Guillemet C. In: Pye LD, La Course WC, Stevens HJ, editors. The physics of non-crystalline solids. London: Taylor and Francis; 1992. p. 55–78.
[12] Kshinka BA, Perrela S, Nguyen H, Bradt RC. Strengths of glass spheres in compression. Journal of American Ceramic Society 1986;69(no. 6):467–72.
[13] Denoual C, Hild F. Dynamic fragmentation of brittle solids: a multi-scale model. European Journal of Mechanics A: Solids 2002;21:105–20.
[14] Yazdchi M, Valliappan S, Zhang W. A continuum model for dynamic damage evolution of anisotropic brittle materials. International Journal of Numerical Methods in Engineering 1996;39:1555–83.
[15] Espinosa HD, Zavattieri PD, Dwivedi SK. A finite deformation continuum/discrete model for the description of fragmentation and damage in brittle materials. Journal of Mechanics and Physics of Solids 1998;46(10):1909–42.
[16] Zavattieri PD, Espinosa HD. Grain level analysis of crack initiation and propagation in brittle solids. Acta Materialia 2001;49:4291–311.
[17] Camacho GT, Ortiz M. Computational modeling of impact damage in brittle materials. International Journal of Solids and Structures 1996;33(20–22):2899–938.

[18] Grujicic M, Pandurangan B, Coutris N, Cheeseman BA, Fountzoulas C, Patel P, et al. A ballistic material model for Starphire®, a soda-lime transparent-armor glass. Materials Science and Engineering – A, in press.

[19] Hild F, Denoual C, Forquin P, Brajer X. On the probabilistic and deterministic transition involved in a fragmentation process of brittle materials. Computers and Structures 2003;81:1241–53.

[20] Brajer X, Gy R, Hild F, Roux S. On the dynamic fragmentation of glass. In: EMMC, tenth European mechanics of materials conference. 2007.

[21] Grujicic M, Pandurangan B, Coutris N, Cheeseman BA, Fountzoulas C, Patel P. A computational investigation of the multi-hit ballistic-protection performance of laminated glass–polycarbonate transparent armor systems. Materials and Design, submitted for publication.